

## Deformation mechanisms and ductile fracture characteristics of a friction stir processed transformative high entropy alloy

S. Sinha<sup>1</sup>, S.S. Nene<sup>1</sup>, M. Frank<sup>1</sup>, K. Liu<sup>1</sup>, R.A. Lebensohn<sup>2</sup>, R.S. Mishra<sup>1\*</sup>

<sup>1</sup>Department of Materials Science and Engineering, Center for Friction Stir Processing, Advanced Materials Manufacturing Processes Institute, University of North Texas, Denton, TX 76207 USA

<sup>2</sup>Theoretical Division, Los Alamos National Laboratory, Los Alamos, NM 87544 USA

\*Corresponding author email: Rajiv.Mishra@unt.edu

### Abstract

Deformation mechanisms of a friction stir processed  $\text{Fe}_{40}\text{Mn}_{20}\text{Co}_{20}\text{Cr}_{15}\text{Si}_5$  transformative high entropy alloy using three different process parameters were studied to explain the microstructural dependence of tensile response in these specimens. The relative strain hardening contribution due to transformation and twinning effects was different for the three different microstructural conditions and thus resulted in different magnitude of work hardening. Crystal plasticity simulations confirmed that synergistic activity of face centered cubic and hexagonal close packed slip and twin mechanisms resulted in sustained work hardening and enhanced uniform elongation. The non-uniform ductility and extent of void nucleation and growth in these specimens were limited. Nevertheless, fractography and X-ray microscopy of fractured tensile specimens verified that microstructural flexibility induced different propensities for void growth and ductile fracture mode. Thus, alloy design induced phase stability, adaptive phase evolution due to friction stir processing, extent and kinetics of martensitic transformation and related work hardening capability of the individual phases combined together to determine the overall tensile response. The crystallographic orientation dependence of deformation induced phase transformation was also thoroughly studied. This study included quantitative determination of the crystallographic orientation where resolved shear stress on leading and trailing partial dislocations favored separation of the partials to cause transformation at a critical value of applied stress.

### Keywords

Martensitic transformation; Tensile behavior; Ductile fracture; Crystal plasticity; Partial dislocation separation

## 1. Introduction

Extensive research in recent years established that during tensile deformation, high entropy alloys with transformation induced plasticity (TRIP-HEAs) show exceptional work hardening behavior, which thus accounts for superior strength-ductility combination [1–5]. These previous studies proved that the enhanced tensile properties can be attributed to the activation of multiple plastic deformation mechanisms. Our earlier studies discussed the tensile behavior of various transformative HEAs, wherein microstructural tailoring through alloy design and thermomechanical processing resulted in enhanced tensile strength-ductility response [6–8]. The TRIP effect in our HEAs is based on face centered cubic (f.c.c.)  $\gamma$  to hexagonal close packed (h.c.p.)  $\varepsilon$ -martensite phase transformation [1–2], although other studies have also discussed TRIP-HEAs involving body centered cubic (b.c.c.) to h.c.p./orthorhombic martensitic transformation [9–10].

This study was a systematic investigation to compare and contrast the deformation mechanisms that ultimately result in different degrees of work hardenability for a particular TRIP-HEA. In order to perform a systematic study, we selected a specific transformative HEA with processing-dependent microstructural flexibility. One of our earlier studies discussed Fe<sub>40</sub>Mn<sub>20</sub>Co<sub>20</sub>Cr<sub>15</sub>Si<sub>5</sub> alloy (CS-HEA), processed by friction stir processing (FSP) using different tool rotation rates [6]. FSP with different tool rotation rates (S350, S150 and D-pass, described in Table 1) led to different phase evolution. Subsequently, these specimens exhibited different tensile response, which was reported in our earlier study [6]. Our aim in the present study was to compare quantitatively the work hardening behavior of the three different microstructural conditions of CS-HEA (responsible for their respective uniform ductility).

Additionally, studies on fracture behavior of TRIP-HEAs are limited. Recently, Wei et al. investigated the fracture mechanisms in a metastable Fe<sub>45</sub>Mn<sub>35</sub>Co<sub>10</sub>Cr<sub>10</sub> HEA [11]. Still, the scope for investigating the fracture mechanisms of TRIP-HEAs is wide. Key to our inquiries is the realization that although transformative HEAs exhibit large uniform ductility due to sustained work hardening response, their non-uniform ductility is quite limited. Such non-uniform ductility represents strain for growth of voids and ductile fracture. Clearly, the ductile failure mechanisms must be distinguished from the deformation mechanisms that contribute to work hardening in the uniform elongation regime. In line with this, Luo and Huang discussed three different types of ductile fracture surfaces: (i) quasi-cleavage (ii) void sheet and (iii) large dimples [12].

Ductile failure can occur by two generic modes, namely plastic instability and void coalescence. Different materials exhibit different mechanisms of ductile fracture by void

nucleation/growth in the absence or presence of necking. Twinning induced plasticity (TWIP) steels undergo failure by localized plastic shear without necking; 304 stainless steel fails by localized plastic shear after necking, while Interstitial Free (IF) steel shows failure by void coalescence with obvious necking [12]. The strain for nucleation and growth of voids has been described based on Considère criterion for plastic instability. Several researchers proposed ductile fracture criteria based on the original or modified Brown and Embury model [13–16] to describe the nucleation and growth of voids. Investigation of void nucleation and growth characteristics is important in elaborating the ductile failure behavior of transformative HEAs.

Therefore, we performed a detailed investigation of the ductile fracture mechanisms of CS-HEA using fractography and X-ray microscopy (XRM). This study seeks to provide a comprehensive overview of the factors contributing to large uniform ductility as well as the reasons for low non-uniform ductility and mode of failure.

## 2. Experimental

The material used in the present investigation was Fe<sub>40</sub>Mn<sub>20</sub>Co<sub>20</sub>Cr<sub>15</sub>Si<sub>5</sub> HEA (CS-HEA). The alloy was produced by vacuum arc-casting in a cold copper crucible using pure metals and ingot dimensions of 300 × 100 × 6 mm<sup>3</sup>. The chamber was backfilled with argon to 1 atm. prior to each melt.

FSP of as-cast CS-HEA sheets was performed using a W-Re tool with shoulder diameter of 12 mm with tapered pin and root diameter, pin diameter and tool length of 7.5 mm, 6 mm and 3.5 mm, respectively. The FSP parameters are listed in Table 1.

**Table 1:** FSP parameters used in the present study

Condition	Pass	Rotational rate (rpm)	Traverse speed (mm/min.)	Plunge Depth (mm)	Tilt Angle (°)
S350	Single	350	50.8	3.65	2.0
S150	Single	150	50.8	3.65	2.0
D-pass	Pass 1	350	50.8	3.65	2.0
	Pass 2	150	50.8	3.70	2.0

Rectangular dog-bone shaped mini-tensile specimens with gage length, gage width and thickness of 5 mm, 1.25 mm and 1 mm, respectively, were machined out using a mini computer numerical control (CNC) machine from 1 mm below the surface within the nugget region of the FSP specimens. Room-temperature tensile tests to failure were performed on a mini-tensile tester

using an initial strain rate of  $10^{-3}$  s<sup>-1</sup>. To check the reproducibility of results, three tests were carried out for each condition.

Electron backscatter diffraction (EBSD) characterization of microstructure was done on a FEI Nova Nano SEM 230 equipped with Hikari Super EBSD detector at an operating voltage of 20 kV. TEAM™ software for EBSD data acquisition and TSL OIM 8 software for EBSD data analysis were used. The EBSD scans of FSP specimens were done at higher magnification than the as-cast condition due to finer grain size in the former. The typical scan area and step size of the EBSD scans for as-cast material were 150  $\mu\text{m} \times 120 \mu\text{m}$  and 0.5  $\mu\text{m}$ , respectively. The corresponding values for the FSP specimens were 39  $\mu\text{m} \times 20 \mu\text{m}$  and 0.1  $\mu\text{m}$ , respectively. Phase fractions reported from EBSD were obtained by averaging three or more scans. Fractography of the fractured tensile specimens were performed using FEI Nova Nano SEM 230 and FEI Quanta 200 ESEM.

X-ray microscopy (XRM) of fractured mini-tensile specimens of CS-HEA was accomplished using a Zeiss Xradia Versa 520 microscope. For each specimen condition, a full field-of-view scan at lower magnification (4X objective) and an interior tomography at higher magnification (20X objective) were carried out to image the fractured half-tensile specimen and detailed fracture surface, respectively. The parameters used for the XRM scans are detailed in Table 2. Voltage and power, exposure time and source to detector distances were optimized depending on the objective, so as to obtain intensity of at least 5000 counts per second. In each case, the filter was selected by checking the transmittance at the angular position of 45°. First, the transmittance with air filter was recorded. Based on that transmittance, the appropriate filter was then selected to increase transmittance in the range of 20–35%. XRM data analysis was carried out using Dragonfly software.

**Table 2:** XRM parameters used to study fracture behavior of CS-HEA

Specimen	S350		D-pass		S150	
<b>Objective</b>	4X	20X	4X	20X	4X	20X
<b>Voltage (kV)</b>	80	80	120	120	120	100
<b>Power (W)</b>	7	7	10	10	10	9
<b>Filter</b>	LE5	LE6	LE5	HE3	HE1	LE6
<b>Binning</b>	2	4	2	4	2	4
<b>Exposure(s)</b>	5	10	1	10	1	10
<b>Source Position (mm)</b>	-30.07	-14.55	-30.60	-16.39	-30.05	-14.57
<b>Detector Position (mm)</b>	30.07	21.75	30.61	25.25	30.05	21.75
<b>Angular range (°)</b>	360	360	360	360	360	360
<b>Number of Projections</b>	1601	3601	1601	3601	1601	3601

### 3. Computational

#### 3.1. Theoretical calculation of dislocation and geometrical hardening

The experimental stress-strain responses for S350, D-pass and S150 specimens were compared with calculated hardening contributions based on dislocation hardening [17-21] and geometrical hardening [22-23]. The original Taylor equation for dislocation hardening is given as,

$$\tau = \tau_0 + \alpha G b \sqrt{\rho} \quad (1)$$

where  $\tau$  is shear flow stress,  $\tau_0$  is shear resistance to dislocation motion when  $\rho \approx 0$ ,  $\alpha$  is a dimensionless material parameter,  $G$  is shear modulus and  $\rho$  is dislocation density. Also, the relationship between shear flow stress  $\tau$  and uniaxial flow stress  $\sigma$  of a polycrystal is  $\sigma = M\tau$  where  $M$  is the Taylor factor. Using these, the Taylor equation can be expressed in the alternate form as,

$$\sigma = \sigma^* + M\alpha G b (\sqrt{\rho} - \sqrt{\rho^*}) \quad (2)$$

where  $\sigma^*$  and  $\rho^*$  are flow stress and dislocation density at the point where the material first becomes plastic. Differentiating Eq. (2) to get the stress evolution with dislocation density yields

$$d\sigma/d\rho = M\alpha G b / 2\sqrt{\rho}. \quad (3)$$

A linear Taylor dislocation hardening can be obtained by considering a constant slope  $(d\sigma/d\rho)_{\text{const}}$ . An initial estimate of  $\rho_{\text{const}} = 10^{12}/\text{m}^2$  was used to calculate the  $(d\sigma/d\rho)_{\text{const}}$ . The values of  $M = 3.1$ ,  $\alpha = 1.16$  [24],  $G = 78 \text{ GPa}$  ( $G = E/(2(1+\nu))$  where  $E = \text{Young's modulus} = 205 \text{ GPa}$  and  $\nu = \text{Poisson ratio} = 0.3$ ) and  $b = 4.3321 \text{ \AA}$  (corresponding to  $\langle c+a \rangle$  system) were applied to calculate  $(d\sigma/d\rho)_{\text{const}}$ . Then the experimental values of stress  $\sigma$  and  $(d\sigma/d\rho)_{\text{const}}$  were used to obtain values of  $\rho$  (dislocation evolution according to a linear Taylor hardening model). Finally, the stress  $\sigma$  according to a linear Taylor hardening model (that is, the  $M\alpha G b \sqrt{\rho}$  contribution as described by Eq. (2)) was calculated using the calculated values of  $\rho$ . The value of  $\rho_{\text{const}}$  used to calculate  $(d\sigma/d\rho)_{\text{const}}$  was refined by iteration until the  $M\alpha G b \sqrt{\rho^*}$  was equal to experimental  $\sigma^*$  (at the yield stress) up to 3 decimal places.

Similarly, the geometric hardening contribution due to crystal lattice rotation with strain was calculated by applying the equation for glide shear strain  $\tau$  given as [25],

$$\tau = (P/A) \sin \chi_0 [1 - \{\sin^2 \lambda_0 / (L_i/L_0)\}]^{1/2} \quad (4)$$

where  $P$  and  $A$  are the applied load and area that specify the applied stress,  $\chi_0$  and  $\lambda_0$  are the angles specifying the initial orientations of the slip plane and slip direction with respect to the tensile (loading) axis,  $L_i$  and  $L_0$  are the instantaneous and original gage lengths, respectively;

hence,  $L_i/L_0$  represents the engineering strain. A range of values of  $\chi_0$  and  $\lambda_0$  based on a theoretical range of possible Schmid factors (e.g., from 0.01 to 0.45) enabled calculating the theoretical geometric hardening contribution.

### 3.2. Visco-plastic self-consistent (VPSC) simulations

The VPSC model simulates the plastic deformation of polycrystalline aggregates based on physical shear mechanisms of slip and twinning and accounts for grain interaction effects [26-27]. Each grain is considered as an ellipsoidal inclusion in a homogeneous medium, where both the inclusion and medium properties are anisotropic. VPSC predicts the macroscopic stress-strain response, thereby accounting for hardening, reorientation and shape change of individual grains to predict the hardening and textural evolution of the material with plastic deformation.

Deformation occurs by slip or twinning when the resolved shear stress reaches a critical value. The extended Voce law [28] given by Eq. (5) describes the evolution of critical stress with deformation,

$$\hat{\tau}^s = \tau_0^s + (\tau_1^s + \theta_1^s \Gamma)(1 - \exp(-\Gamma|\theta_0^s/\tau_1^s|)) \quad (5)$$

where  $\Gamma = \sum_s \Delta\gamma^s$  is the accumulated shear in the grain, and  $\tau_0$ ,  $\theta_0$ ,  $\theta_1$ ,  $(\tau_0+\tau_1)$  are the initial critical resolved shear stress (CRSS), initial hardening rate, asymptotic hardening rate and back-extrapolated CRSS, respectively. Additionally, self and latent hardening are allowed by defining coupling coefficients ( $h^*$ ) to account for the interactions between slip/twin systems.

In the present study, VPSC simulations of uniaxial tensile deformation of S350, S150 and D-pass conditions of CS-HEA were performed to obtain insight into the relative propensities of slip and twin modes, to explain the differences in work hardening behavior. The initial textures (in the form of Euler angles  $(\phi_1, \phi, \phi_2)$ ) of as-FSP condition of S350, S150 and D-pass specimens obtained from EBSD were used as input for the VPSC simulations. Phase fractions of  $\gamma$  (f.c.c.) and  $\epsilon$  (h.c.p.) derived from EBSD were also specified as input (S350: 5%  $\gamma$  + 95%  $\epsilon$ , S150: 65%  $\gamma$  + 35%  $\epsilon$ , D-pass: 31%  $\gamma$  + 69%  $\epsilon$ ). To obtain appropriate Voce parameters  $(\tau_0, \tau_1, \theta_0, \theta_1)$  to model the hardening behavior, initially we started with hardening parameters reported for TWIP steels for the  $\gamma$  (f.c.c.) phase [29] and conventional h.c.p. metals like Mg/Ti for the  $\epsilon$  (h.c.p.) phase [30-33]. The Voce parameters were changed and refined by comparing the simulated stress-strain response for each specimen condition with the corresponding experimental curves (with every new set of  $(\tau_0, \tau_1, \theta_0, \theta_1)$ ). This refinement was repeated until a reasonably good match was obtained between experimental and simulated curves for each specimen condition (S350, S150 and D-pass). Then, VPSC simulations were performed for all three conditions using

the Voce and latent ( $h^*$ ) hardening parameters listed in Table 3. Note that the  $\gamma$  (f.c.c.) phase is assumed to be softer than the  $\epsilon$  (h.c.p.) phase (Table 3) because previous researchers showed through first-principles calculations [34] and experimental micro-hardness measurements [35] that the f.c.c. phase is softer than the h.c.p. phase in HEAs.

**Table 3:** Voce and latent hardening parameters used in the present study

Specimen	Mode	$\tau_0$ (MPa)	$\tau_1$ (MPa)	$\theta_0$ (MPa)	$\theta_1$ (MPa)	$h^{*,1}$	$h^{*,2}$	$h^{*,3}$	$h^{*,4}$	$h^{*,5}$	$h^{*,6}$
S350	1	275	200	300	50	1	1.4	-	-	-	-
	2	370	200	300	100	1	1.4	-	-	-	-
	3	470	40	340	60	-	-	1	1	10	2
	4	490	50	390	80	-	-	1	1	10	2
	5	540	60	1200	40	-	-	1	1	2	2
	6	530	60	1000	20	-	-	1	1	10	16
S150	1	275	200	300	50	1	1.4	-	-	-	-
	2	370	200	300	100	1	1.4	-	-	-	-
	3	730	100	900	80	-	-	1	1	10	2
	4	750	110	1000	100	-	-	1	1	10	2
	5	800	50	2500	40	-	-	1	1	2	2
	6	790	50	2000	60	-	-	1	1	10	16
D-pass	1	275	200	300	50	1	1.4	-	-	-	-
	2	370	200	300	100	1	1.4	-	-	-	-
	3	450	60	330	100	-	-	1	1	10	2
	4	470	70	380	120	-	-	1	1	10	2
	5	520	80	1200	80	-	-	1	1	2	2
	6	510	80	1000	60	-	-	1	1	10	16
<b>Description of modes</b>						<b>Initial grain shape (initial ellipsoid ratios)</b>					
1: FCC $\{111\} < \bar{1}\bar{1}0 >$ Slip						S350: 5:1:1 for fcc and 1:1:1 for hcp					
2: FCC $\{111\} < \bar{1}\bar{1}\bar{2} >$ Twin						S150 and D-pass: 1:1:1 for both fcc and hcp					
3: HCP $\{10\bar{1}0\} < 11\bar{2}0 >$ Prismatic Slip						<b>Phase fractions</b>					
4: HCP $\{0001\} < \bar{1}\bar{1}\bar{2}0 >$ Basal Slip						S350: 5% fcc + 95% hcp					
5: HCP $\{10\bar{1}1\} < 11\bar{2}3 >$ Pyramidal $\langle c+a \rangle$ Slip						S150: 65% fcc + 35% hcp					
6: HCP $\{10\bar{1}2\} < 10\bar{1}1 >$ Extension Twin						D-pass: 31% fcc + 69% hcp					

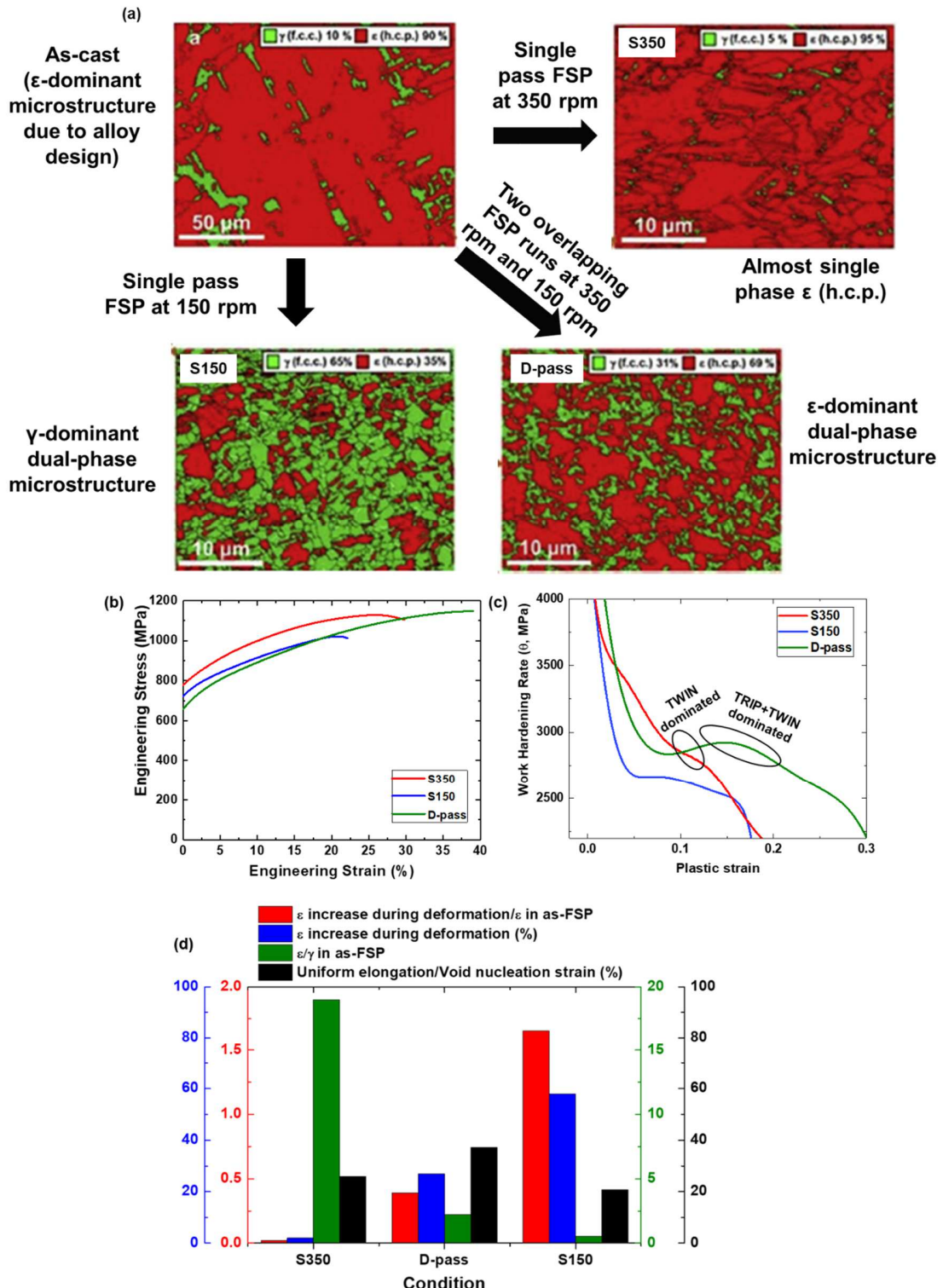
## 4. Results

### 4.1. Uniform ductility and work hardening mechanisms

CS-HEA has  $\epsilon$  (h.c.p.) dominant dual-phase microstructure in the as-cast condition (Fig. 1 (a)). The phase evolution in as-FSP specimens is different for the different FSP parameters (S350, S150 and D-pass), and results in three different microstructures (Fig. 1 (a)). S350 yields almost single-phase  $\epsilon$  (h.c.p.) microstructure, S150 has  $\gamma$  (f.c.c.) dominant dual-phase microstructure, while D-pass specimen displays  $\epsilon$  (h.c.p.) dominant dual-phase microstructure.

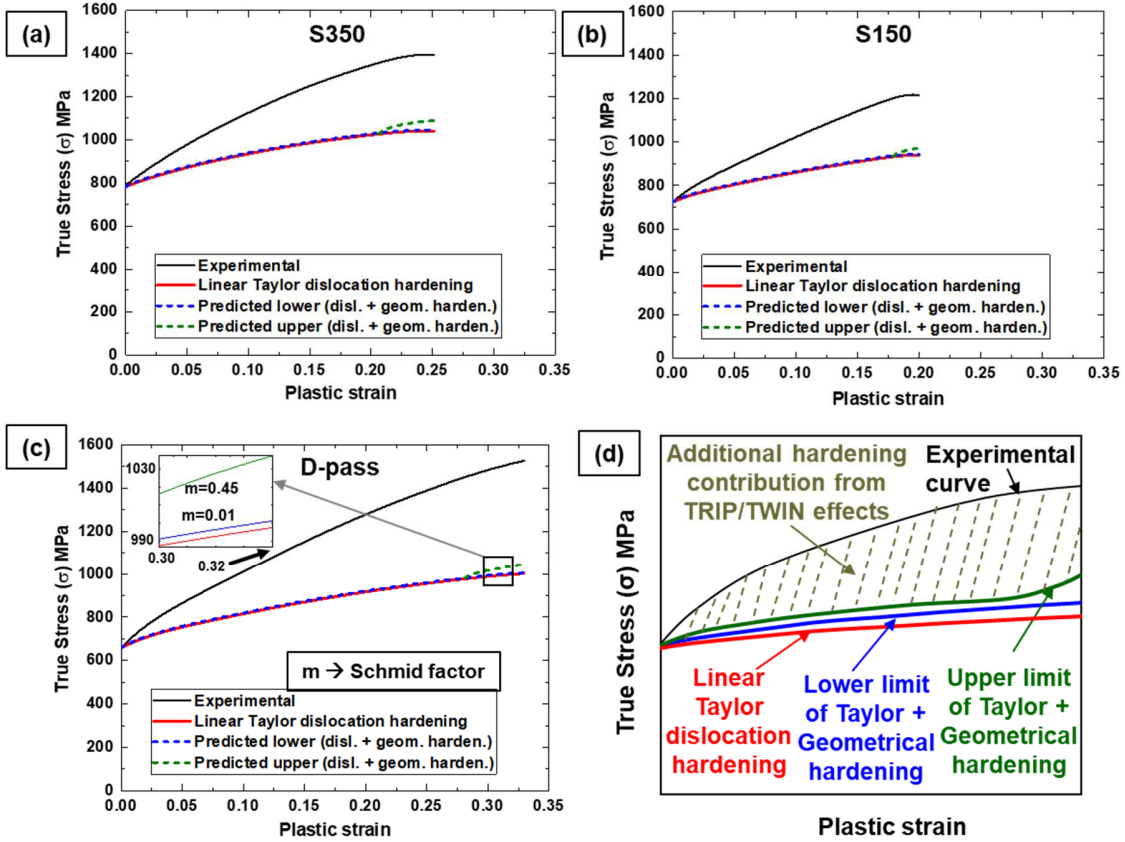
The corresponding tensile and strain hardening curves are included in Figs. 1 (b) and (c), respectively. Note that the comparison of the tensile response of as-FSP specimens with that of as-cast specimen was discussed in our earlier study [6]. Among the as-FSP specimens, D-pass condition exhibits the highest tensile elongation, while S150 shows the lowest ductility. The higher elongation to failure of D-pass specimen is attributed to higher, sustained strain hardening due to TRIP and twinning [6].

Figure 1 (d) presents a comparison of the  $\varepsilon$  (h.c.p.) fraction change from as-FSP to deformed condition for the three processing conditions (S350, S150 and D-pass), and the corresponding uniform elongation (which also corresponds to the void nucleation strain related to the onset of plastic instability). Clearly, the uniform elongation is dependent on the interplay between the amounts of  $\varepsilon$  (h.c.p.) already present in the as-FSP microstructure and  $\varepsilon$  (h.c.p.) formed due to transformation, as well as the work hardening characteristics of deformed  $\varepsilon$  (h.c.p.). The fact that the D-pass specimen shows the highest uniform elongation indicates that the  $\gamma$  (f.c.c.) phase stability is an important factor. Conceptually, if the alloy is more metastable, the TRIP stress would be lower and backstresses would not be able to hinder transformation. CS-HEA is highly metastable due to alloy design. Now, considering that S350 has a higher  $\varepsilon/\gamma$  ratio than the D-pass in the as-FSP condition (Fig. 1 (d)), we can infer that pronounced TRIP effect in D-pass condition contributes to highest work hardening and uniform ductility. Also, the high work hardening in D-pass condition is due to the ductile nature of the  $\varepsilon$  (h.c.p.) phase itself. S150 condition has  $\gamma$  (f.c.c.) dominant microstructure in the as-FSP condition, and exhibits significant  $\varepsilon$  (h.c.p.) phase formation during deformation (value for the ratio of  $\varepsilon$  increase during deformation and  $\varepsilon$  in as-FSP as shown in Fig. 1 (d)). Yet, S150 shows lowest work hardening and uniform elongation. This is because the kinetics of transformation also influences the deformation capability of the phases. The relative activity of slip modes and amount of twinning of the  $\gamma$  (f.c.c.) and  $\varepsilon$  (h.c.p.) phases are important and will be discussed later from VPSC simulation results. First, we must distinguish among the three specimen conditions based on the extent of work hardening. Even though TRIP/twin effects contribute to work hardening in all three specimen conditions, the degree of work hardening in these specimens is different. Clearly, the relative contribution from TRIP/twin effects is different for each specimen condition. The following discussion seeks to explain the difference in hardening contributions for S350, D-pass and S150 specimens to justify the different extents of work hardening observed.



**Fig. 1.** (a) EBSD phase fraction maps, (b) tensile curves [6], (c) strain hardening curves [6], and (d) comparison of  $\epsilon$  (h.c.p.) phase fraction change during deformation and uniform elongation/Void nucleation strain (%) for the various FSP conditions.

The predicted curves based on the sum of linear Taylor dislocation hardening and geometrical hardening are plotted along with the experimental curves for S350, S150 and D-pass conditions in Figs. 2 (a), (b) and (c), respectively. Figure 2 (d) illustrates the common features of Figs. 2 (a)–(c) to explain the difference between experimental and theoretical hardening contributions. Clearly, the small geometrical hardening contribution explains why the predicted curves of dislocation plus geometrical hardening almost overlap with the dislocation hardening line in Figs. 2 (a)–(c). Interestingly, the additional hardening contribution from TRIP/twin effects (corresponding to the region shaded by golden dotted lines in the schematic Fig. 2 (d)) is different for the different specimen conditions in Figs. 2 (a)–(c). The calculated linear Taylor dislocation hardening simply represents what would be the hardening arising solely out of the evolution of dislocation content. Similarly, the geometrical hardening estimates the theoretical hardening possible due to lattice reorientation with strain. On the other hand, the additional work hardening (difference between experimental and calculated curves) arises from strain induced by f.c.c. to h.c.p. transformation, backstress generated in the dual-phase microstructure and load partitioning to the martensite phase, thus accounting for the microstructure and stress-state dependence of the work hardening behavior. Figs. 2 (a)–(c) clearly show that the D-pass specimen exhibits the highest additional hardening contribution from TRIP/twin ( $\sim 500$  MPa at the UTS). The corresponding values for S350 and S150 specimens are  $\sim 300$  MPa and  $\sim 200$  MPa, respectively. Thus, the relative work hardening contributions from TRIP/twin effects are quantified for the different specimen conditions. The lowest TRIP/twin hardening contribution for S150 specimen is due to the fact that kinetics of TRIP is very fast whereas the S350 deforms completely with different preferential strain accommodation mechanisms. Also, it must be mentioned that the stored dislocation density and grain size of the  $\gamma$  (f.c.c.) phase in S150 and D-pass conditions alter the kinetics of TRIP.



**Fig. 2.** Calculated hardening contributions in comparison with experimental curves for (a) S350, (b) S150, and (c) D-pass specimens of CS-HEA. (d) A schematic to explain the various hardening contributions and the gap that needs further discussion.

#### 4.2. VPSC simulations of stress-strain response

S350, S150 and D-pass conditions of CS-HEA exhibit different degrees of work hardening due to the synergistic effect of alloy chemistry induced phase stability, adaptive phase evolution due to FSP parameters and propensity and kinetics of  $\gamma$  (f.c.c.) to  $\varepsilon$  (h.c.p.) martensitic transformation. Various factors like phase ratio in the as-FSP state, TRIP stress, rate of phase transformation, stored dislocation content and grain size of  $\gamma$  (f.c.c.) influence the deformability of the  $\gamma$  (f.c.c.) and  $\varepsilon$  (h.c.p.) phases. Therefore, quantifying the relative activity of f.c.c. and h.c.p. deformation mechanisms in each specimen condition is necessary to get a holistic overview of the factors contributing to the different work hardening behaviors.

VPSC simulations were performed to quantify the relative contribution of deformation modes in S350, S150 and D-pass specimens. Figs. 3 (a)–(c) show the VPSC simulated stress-strain curves for S350, S150 and D-pass specimens along with corresponding experimental curves. The activity of a deformation mode refers to the sum over all grains of shear rates

contributed by that mode, weighted by grain volume fraction [36-37]. The sum of all mode activities is the total activity. Thus, the relative activity of each slip/twin mode can be obtained by the ratio of activity of each mode to the total activity. Since the relative activity of slip and twin modes cannot be directly measured experimentally, crystal plasticity simulations were used to predict the same. It is worth mentioning here that, interrupted tensile tests supplemented with EBSD at different strain levels or in-situ tensile-EBSD experiments could provide valuable insight to validate some features, such as the changes in dislocation density or crystal textures. Figures 3 (d), (e) and (f) show the variation of relative activities of all f.c.c. and h.c.p. slip and twin modes for S350, S150 and D-pass specimens, respectively. The activity curves confirm that the f.c.c. slip activity decreases with progressive strain, while the h.c.p. pyramidal  $\langle c+a \rangle$  slip activity increases significantly with increasing strain. S350 has predominantly higher activity for h.c.p. pyramidal  $\langle c+a \rangle$  slip than all the other modes (Fig. 3 (d)). S150 shows the highest activity for f.c.c. slip, and h.c.p. pyramidal  $\langle c+a \rangle$  slip is the second most significant mode (Fig. 3 (e)). Interestingly, in the D-pass specimen, f.c.c. slip and h.c.p. pyramidal  $\langle c+a \rangle$  slip activities are comparable (Fig. 3 (f)). Also, the activities of these two modes are relatively closer to the other modes like h.c.p. basal and prismatic slip, compared to S350 or S150. For example, S150 shows much higher f.c.c. slip activity than h.c.p. modes (Fig. 3 (e)), but fails to produce significant work hardening. S350 features high activity of h.c.p. pyramidal  $\langle c+a \rangle$  slip but f.c.c. slip activity is low even at low strain (Fig. 3 (d)), because the as-FSP volume fraction of  $\gamma$  (f.c.c.) phase is low in this condition (Fig. 1 (a) and Table 3). As a result, work hardening of S350 is better than S150, but lower than the D-pass specimen. Only the D-pass specimen shows synergistic activity of f.c.c. and h.c.p. deformation modes (Fig. 3 (f)). This confirms that dual-phase strain partitioning is effectively achieved in the D-pass condition, thereby resulting in a sustained work hardening response. In an earlier study, we sought to estimate the relative hardness of  $\gamma$  (f.c.c.) and  $\varepsilon$  (h.c.p.) phases in CS-HEA from nanoindentation measurements [38]. That study showed that both the phases in a dual-phase microstructure have similar hardness and modulus. While a thorough independent investigation is required to truly differentiate the intrinsic deformability of the two phases in this alloy, the similarity in nanoindentation response of both phases indicated synergistic hardening/softening of the two phases in the microstructure, depending on thermo-mechanical processing or deformation state. This further strengthens our hypothesis that the synergistic hardening effect of the  $\gamma$  (f.c.c.) and  $\varepsilon$  (h.c.p.) phases is the key to sustained work hardening response in CS-HEA.

Figure 3 (g) displays the average active systems per grain (AVACS) as a function of strain for the f.c.c. and h.c.p. phases in all three specimens. The f.c.c. phase in all three specimens shows an initial increase in AVACS followed by saturation of AVACS at higher strain. The initial increase in AVACS is attributed to  $\gamma$  (f.c.c.) twinning, while at higher strain, twinning activity saturates and hence, there is saturation in AVACS [39]. On the other hand, initially the h.c.p. phase decreases in AVACS after which it increases with increasing strain. Since  $\epsilon$  (h.c.p.) twinning and pyramidal  $\langle c+a \rangle$  slip are operative at higher strain to accommodate strain according to von Mises criterion, AVACS increases for  $\epsilon$  (h.c.p.) phase at high strain. The key observation here is that AVACS increases most steeply for the S350 condition in the case of f.c.c. phase and for the S150 condition in the case of h.c.p. phase. In other words, the less dominant phase in each case undergoes rapid increase in AVACS. This is because the strain in the less dominant phase is mostly determined or imposed by the majoritarian phase to fulfill compatibility, therefore requiring higher AVACS consistent with a Taylor-like behavior. This also confirms that the metastability based alloy design induced phase evolution can alter the individual deformation responses of the two phases and the deformability of the phases is not just dependent on crystal structure.

Figure 3 (h) shows the f.c.c. and h.c.p. twin volume fractions as a function of strain for S350, S150 and D-pass conditions. D-pass specimen has the highest  $\epsilon$  (h.c.p.) twin fraction, while S350 specimen also exhibits  $\gamma$  (f.c.c.) and  $\epsilon$  (h.c.p.) twinning. Therefore, the twin fraction evolution from VPSC confirms the contribution of twinning to work hardening response (Fig. 1 (c)). The good work hardening capability of S350 is due to twinning-induced increase in strain hardening. The highest work hardening capability of D-pass specimen is attributed to the combination of TRIP and  $\epsilon$  (h.c.p.) twinning. The VPSC simulations confirm that D-pass condition has the highest propensity of  $\epsilon$  (h.c.p.) twinning. In line with this, stacking fault energy (SFE) is an important factor that influences the ease of twinning. In the present case, we are comparing three different microstructural states of the same alloy (CS-HEA). The SFE of our CS-HEA alloy was determined to be  $\sim 6.31$  mJ/m<sup>2</sup> using in-situ neutron diffraction in another study by Frank et al. [40]. This level of SFE is designed to favor  $\epsilon$ -martensite transformation, while the typical SFE range for twinning is slightly higher than that of transformation. We can predict that there was some variation in the SFE between the S350, D-pass and S150 conditions of CS-HEA due to the microstructural diversity. As a result, the phase fractions in as-FSP state and the amount of  $\gamma$  (f.c.c.)  $\rightarrow$   $\epsilon$  (h.c.p.) transformation occurring upon tensile deformation are

different. Similarly, the ease of twinning was also different for the three different specimen conditions.

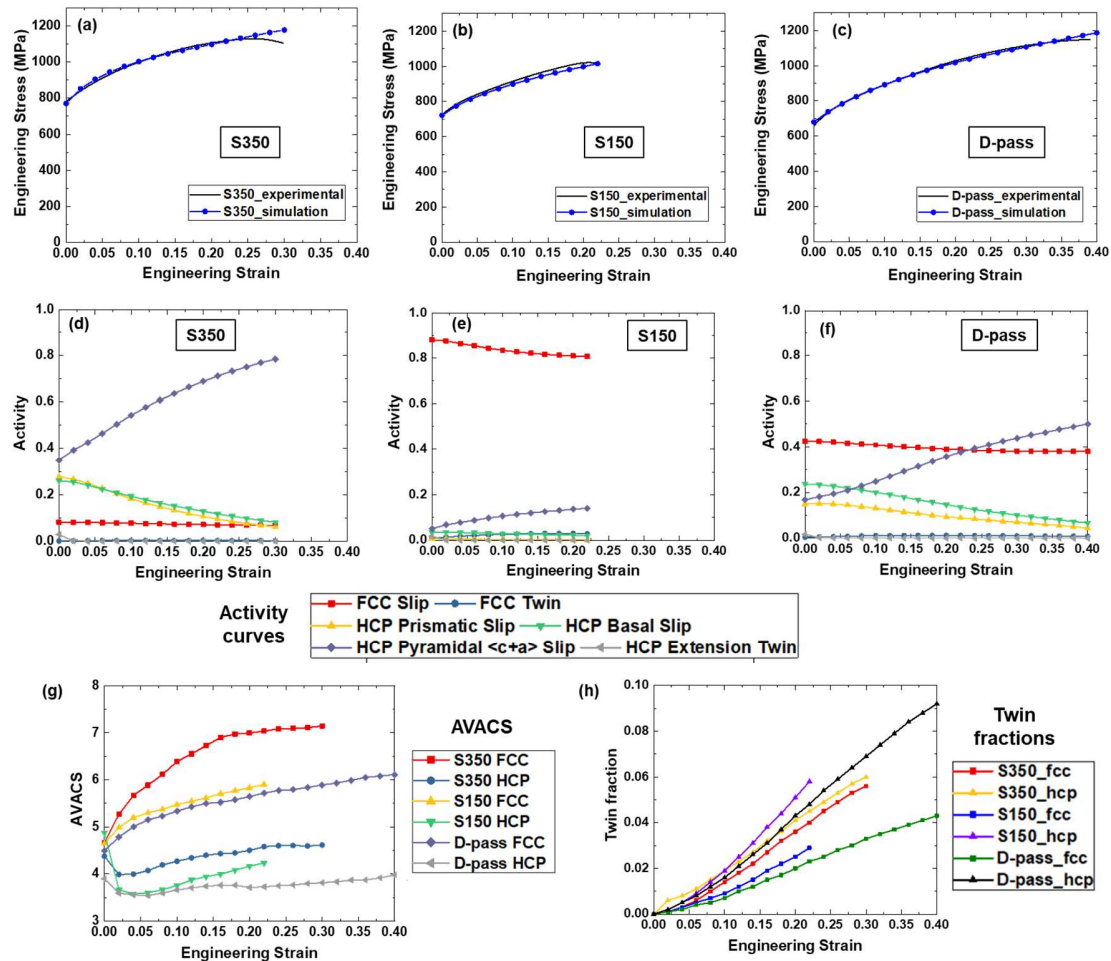


**Fig. 3.** VPSC simulation results. Simulated stress-strain curves in comparison with experimental curves for (a) S350 (b) S150 (c) D-pass conditions. Corresponding activity of all deformation modes as a function of strain for (d) S350 (e) S150 (f) D-pass conditions. Evolution of (g) average active slip systems (AVACS) and (h) twin volume fractions with strain for f.c.c. and h.c.p. phases in all the three conditions.

#### 4.3. Non-uniform ductility and fracture mechanisms

Despite large uniform elongation, the CS-HEA specimens have very little non-uniform ductility (post-necking). Figure 1 (b) confirms very small non-uniform ductility region in S350 and S150 specimens, while the D-pass condition contains no non-uniform ductility at all. While uniform elongation depends on work hardening behavior, non-uniform ductility corresponds to

the growth of voids and fracture mechanisms. Therefore, the failure mechanisms of these CS-HEA specimens were investigated separately by fractography and X-ray microscopy.

Figure 4 shows the fractography of S350, D-pass and S150 specimens of CS-HEA. S350 specimen exhibits mixed mode failure, wherein ductile regions are interspersed with brittle faceted regions throughout the fracture surface (Fig. 4 (a2)). While Fig. 4 (a1) shows a higher magnification image of a ductile region, Fig. 4 (a3) displays a brittle faceted region. The ductile regions contain characteristic dimples, with voids within the dimples. The typical size of voids/dimples is of the order of  $1.2 \pm 1.0 \mu\text{m}$ . Unlike mixed mode fracture in S350 specimen, both D-pass and S150 specimens show only ductile failure features. The fracture surface of D-pass specimen consists of coarse dimpled region and fine dimpled region demarcated clearly by the surface along which the two halves of the tensile specimen separated (Fig. 4 (b2)). Fine voids/cavities are observed within both the regions containing fine dimples (Fig. 4 (b1)) as well as the coarse dimpled region (Fig. 4 (b3)). S150 specimen is characterized by formation of large cavities within the surface consisting of dimples/voids (Figs. 4 (c1-c3)). This indicates a higher propensity for cavity-driven failure. The average size of dimples/voids is  $4.4 \pm 2.7 \mu\text{m}$ , while the characteristic elongated (near elliptical) cavities are  $9.1 \pm 2.6 \mu\text{m}$  long and  $3.7 \pm 1.2 \mu\text{m}$  wide.

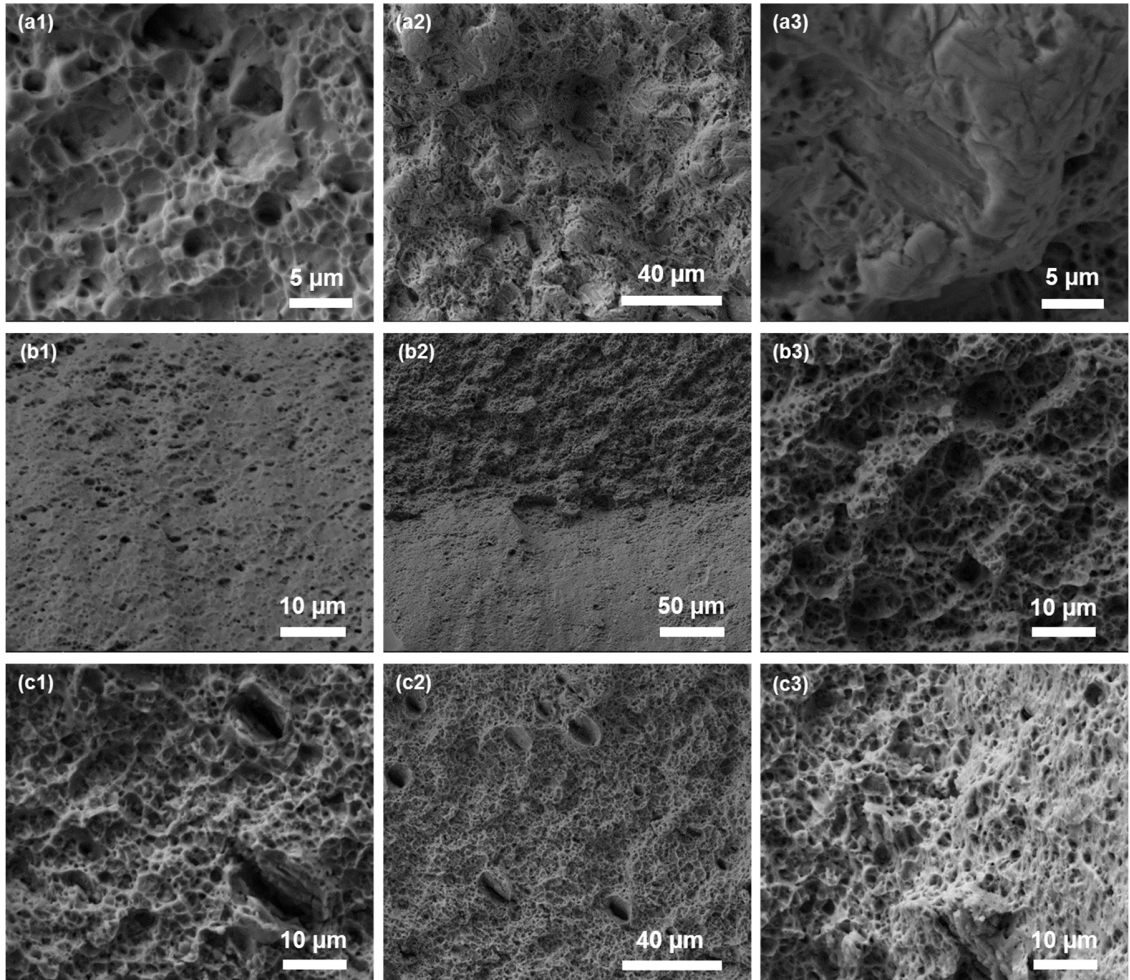


**Fig.4.** Fractography of CS-HEA tensile specimens, (a1-a3) S350 condition, (b1-b3) D-pass condition, and (c1-c3) S150 condition.

Figures 5 (a)–(c) are SEM images of the fractured tensile specimens of S350, D-pass and S150 conditions of CS-HEA. Distinct necking is not observed in these specimens due to the absence of significant non-uniform ductility. Figures 5 (d), (e1) and (f) are low magnification XRM images of the failed tensile specimens. S350 specimen has a dimpled fracture surface interspersed with faceted regions (Fig. 5 (d)), similar to that observed from SEM fractography. The distinct separation of the two tensile halves of D-pass specimen is indicated clearly by the XRM image in Fig. 5 (e1). Low magnification SEM fractography of both halves (Figs. 5 (e2)–(e3)) also indicates that the initiation of necking led to immediate failure in the D-pass specimen, thus creating a distinct separation interface between the two halves. Therefore, clearly, although the D-pass specimen showed highest uniform ductility due to sustained work hardening, the

sudden failure at post-necking was due to the inability to accommodate non-uniform strain. Figure 5 (f) confirms that some cracks along the gage length are observed in the S150 specimen.

Higher magnification XRM images (Figs. 5 (g)–(i)) reveal the dimpled rupture characteristics of the fracture surface. The inclined surface of S350 specimen with bigger dimples suggests that the separation of the two tensile halves occurred along the surface profile of the dimpled surface. In comparison, D-pass and S150 specimens show relatively flatter surfaces with smaller dimples. The dimpled fracture surfaces of each specimen were extracted as a mesh (green surfaces in Figs. 5 (g)–(i)) to quantify the dimple characteristics of each specimen. The quantitative dimple characteristics plotted for the three specimen conditions appear in Fig. 6 (a). Dimples with height of the order of 20–30  $\mu\text{m}$  are observed in S350 specimen, while D-pass and S150 specimens have smaller dimples typically of the height of 5–10  $\mu\text{m}$ . On the other hand, D-pass specimen shows the highest dimple density ( $\sim 107824 / \text{mm}^2$ ); and corresponding to the highest dimple frequency, the average area covered by each dimple is lower ( $\sim 9.3 \mu\text{m}^2$ ) than S350 and S150 specimens.

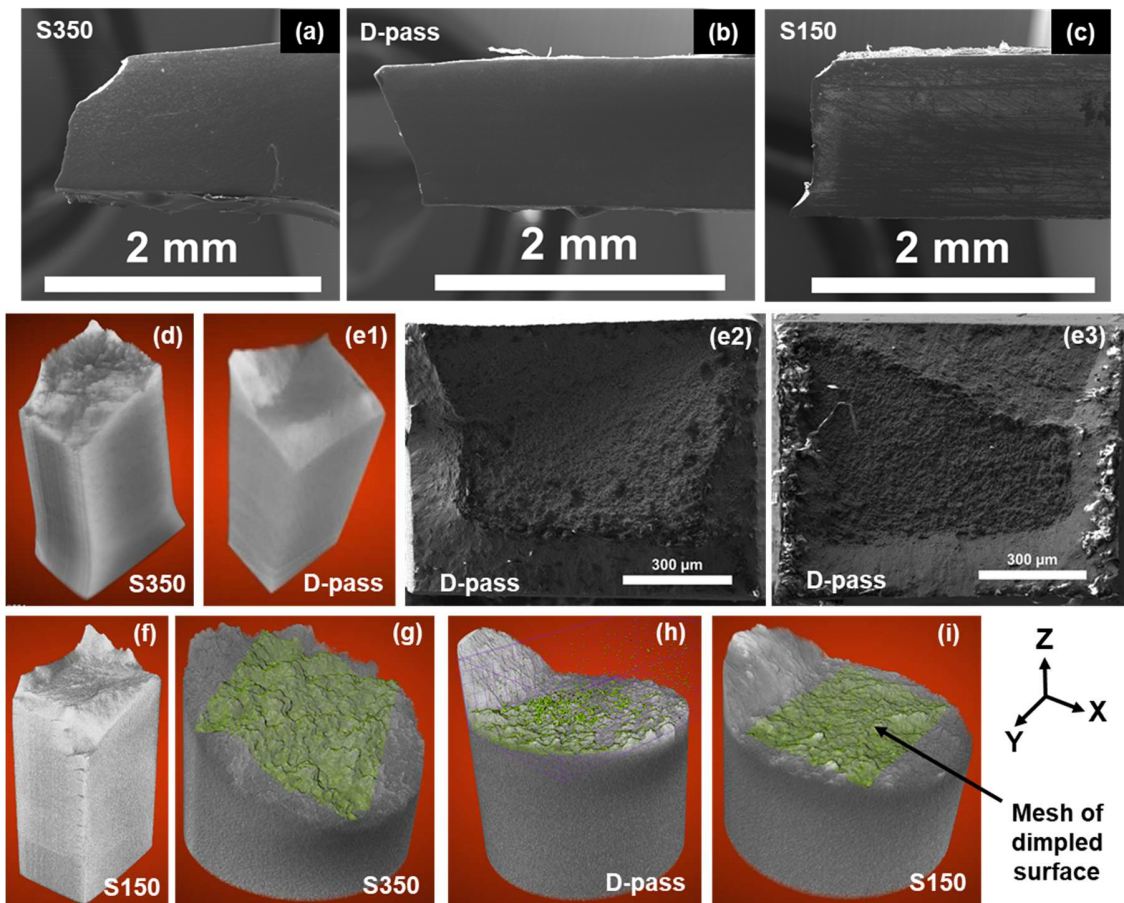


**Fig. 5.** (a), (b), (c) SEM images of fractured tensile specimens, (d), (e1), (f) low magnification XRM images, (e2) and (e3) SEM images of fracture surface of both halves of D-pass tensile specimen, and (g), (h), (i) higher magnification XRM images with superimposed mesh extracted for dimple analysis (CS-HEA specimen conditions labeled on each image).

Vertical 2D slices obtained from XRM were used to observe the void characteristics beneath the fracture surface. Some representative slices for each specimen condition are displayed in Figs. 6 (b)–(d), while the void area fraction obtained from these slices is plotted in Fig. 6 (a). The S350 specimen shows void formation beneath the fracture surface (Fig. 6 (b1)–(b2)). Such voids as observed in several 2D slices confirm the occurrence of void nucleation and some void growth during the ductile fracture process. In contrast, only one significantly large void was observed beneath the fracture surface in the D-pass specimen (slice no. 220 in Fig. 6 (c2) out of 472 slices). Moreover, the fracture surface of this specimen also showed much finer voids without void growth/coalescence. Therefore, void growth was clearly inhibited in the D-pass specimen, consistent with the total absence of any non-uniform ductility and immediate failure after initiation of necking. XRM 2D slices of S150 specimen (Fig. 6 (d1)–(d2)) displaying several elongated cavities even beneath the fracture surface confirm the cavity-driven failure propensity of this specimen. Overall, S350 specimen showed highest void area fraction (~2%), while D-pass specimen showed lowest void area fraction (Fig. 6 (a)). Correlating void formation with starting microstructure, we can conclude that the D-pass specimen with  $\epsilon$ -dominant dual-phase microstructure nucleates fine voids without scope for void growth; the S350 specimen with almost single-phase  $\epsilon$  (h.c.p.) phase shows void growth, while large cavities are formed in the S150 specimen with  $\gamma$ -dominant dual-phase microstructure.

With regard to mechanisms driving the nucleation of voids, ductile rupture initiation by void nucleation at inclusions or precipitates and second-phase particles is well known [13-14]. Noell et al. discussed a mechanism of nucleation of voids in pure Ta by vacancy condensation at deformation-induced boundaries such as cell block boundaries and mentioned that this mechanism is not restricted to pure metals, but is also possible at microstructural features in two-phase materials [41]. They also observed that some incipient subsurface voids nucleated by this mechanism. Therefore, the possible void nucleation sites are the phase interfaces, grain boundaries or deformation-induced boundaries such as cell block boundaries, triple junctions or twin intersections [41].

The fracture behavior study completes the analysis of the overall tensile response of S350, S150 and D-pass specimens of CS-HEA. D-pass specimen has the best uniform elongation due

to sustained work hardening by TRIP/twin effects. However, failure initiates soon after necking without any non-uniform ductility. The failure occurs by ductile fracture characterized by high dimple density but with limited scope for void growth. The absence of void growth explains the total absence of non-uniform ductility. In contrast, S150 specimen has inferior work hardening response because high TRIP kinetics inhibits the work hardening capability due to TRIP effects. Also, S150 has a high propensity for cavity-driven failure. This is also attributed to significant amount of  $\gamma$  (f.c.c.) to  $\epsilon$  (h.c.p.) transformation with high TRIP kinetics. Higher frequency of  $\gamma/\epsilon$  interfaces result in more cavity nucleation sites and large cavities are formed at sites where fast TRIP kinetics does not allow sufficient time to accommodate the strain mismatch between the phases. As a result, the overall tensile response of S150 condition is inferior compared to S350 and D-pass. The reasonably good twinning-induced work hardening of the S350 specimen accounts for higher uniform elongation than S150. However, mixed mode failure occurs characterized by traditional cleavage brittle fracture regions as well as ductile regions with large dimples. The dominance of brittle cleavage fracture regions limits the non-uniform ductility although this specimen manifests some capability for accommodating non-uniform strain characterized by void growth. Thus, the overall tensile response of S350 is better than S150 but inferior to D-pass condition.

In summary, the present study revealed that the D-pass specimen of CS-HEA exhibited the best strength-ductility combination due to sustained work hardening based on the synergistic effect of f.c.c. and h.c.p. deformation. From a materials design point of view, the study provides the following generic insight. For sustained work hardening by synergistic deformation, the microstructure must be tailored to obtain a dual-phase nanocrystalline microstructure where the usually harder phase between the two is the dominant phase, yet there is a significant fraction of the intrinsically softer phase. This microstructural variant can be achieved by tuning the alloy chemistry as well as thermo-mechanical processing. When the fractions of both phases are comparable (not near single-phase before tensile deformation), the dual-phase strain partitioning and strain compatibility requirements enable the simultaneous work hardening of both phases. Although one phase is supposed to be intrinsically softer than the other, the hardness/modulus and work hardenability/deformability of the phases in such a microstructure are more compatible. Also, the mechanism of transformation induced plasticity due to deformation-induced phase transformation and increase in work hardening induced by multiple deformation twinning and slip mechanisms are integral to obtain such sustained work hardening response. Again, this is to be achieved by combining alloy design with thermo-mechanical processing;

wherein, alloy design is used to modulate the stacking fault energy to favor transformation and subsequent twinning, while the constituent phases must deform by multiple mechanisms whose hardening propensity could be influenced by prior thermo-mechanical processing. At the same time, the transformation kinetics must allow sufficient time to accommodate the strain mismatch between the phases; otherwise the propensity to nucleate cavities would increase. For the same reason, the transformation product phase must be the dominant phase of the dual-phase microstructure and not the other way round. If the transformation parent phase fraction is higher in the initial microstructure (before tensile deformation), that would increase the frequency of phase interfaces that would act as potential cavity nucleation sites during tensile deformation when the transformation kinetics is too fast to allow the accommodation of the strain mismatch between the phases; and significant cavity nucleation could limit the ductility.

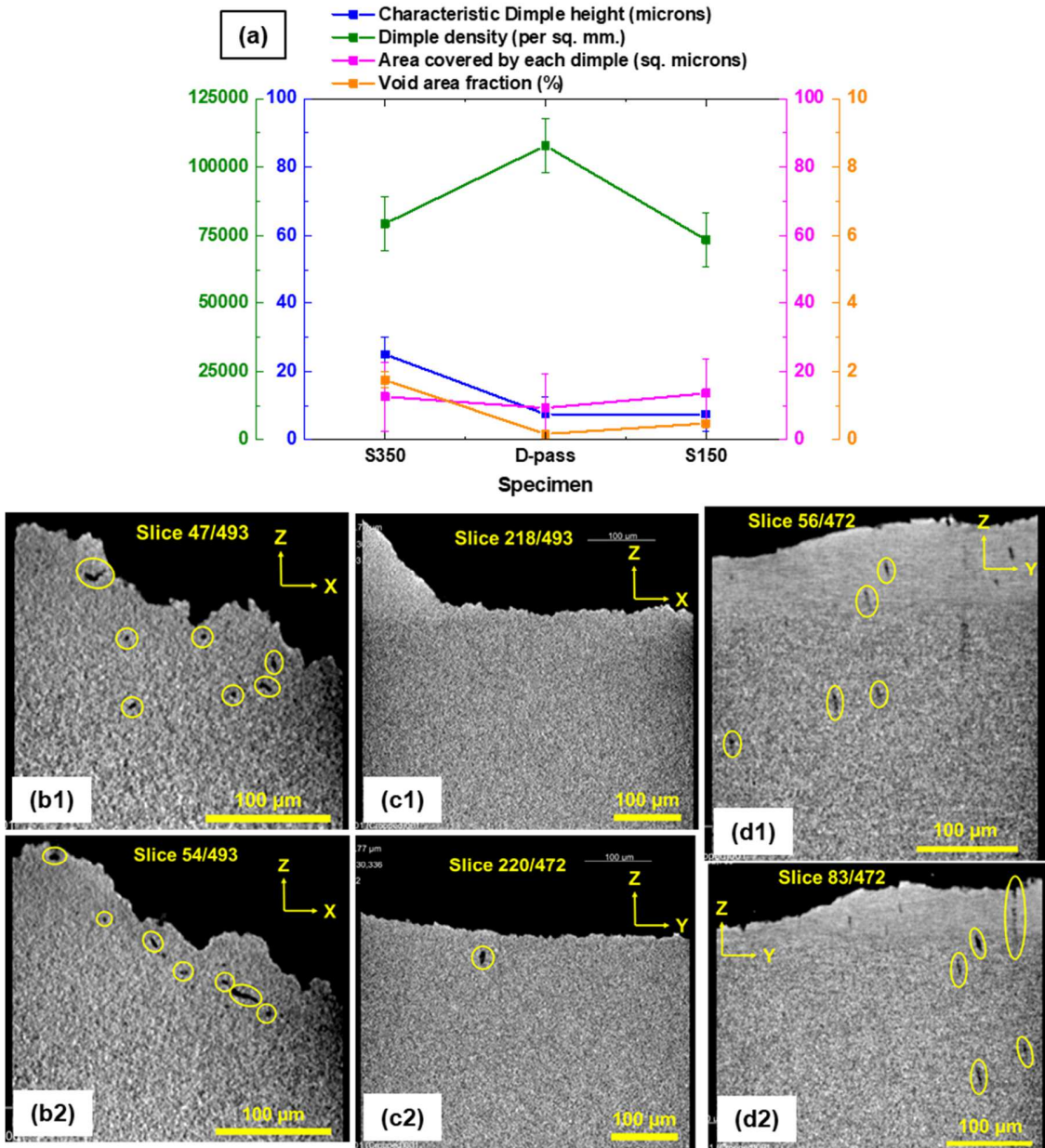


**Fig. 6.** (a) Dimple and void analysis from XRM of fractured tensile specimens. Representative XRM 2D slices showing voids/cavities for (b1)–(b2) S350 specimen, (c1)–(c2) D-pass specimen, and (d1)–(d2) S150 specimen of CS-HEA.

## 5. Discussion

### 5.1. Orientation dependence of resolved shear stress

The results in Section 4.1 proved that the amount of transformation/twinning induced work hardening significantly contributes to the strength-ductility response of CS-HEA. Therefore, an important question that follows is what causes a  $\gamma$  (f.c.c.) grain to transform to  $\epsilon$  (h.c.p.) during

deformation. This is fundamentally based on the fact that in f.c.c. metals, perfect dislocations dissociate into Shockley partials leaving a stacking fault (SF) between them [42]. The effect of applied stress on the separation distance between partials is as strong as the effect of SFE [42]. Deformed microstructures of austenitic stainless steels often show SF ribbons with 1  $\mu\text{m}$  separation between the two partials [42].

Polatidis et al. discussed that when the leading partial dislocation (LPD) has higher Schmid factor ( $m$ ) than the trailing partial dislocation (TPD), the separation between the partials increases due to applied stress, resulting in local formation of  $\epsilon$  (h.c.p.) martensite phase [43]. Additionally, resolved shear stress (RSS) or Schmid factor depends on  $\gamma$  (f.c.c.) grain orientation with respect to the applied stress direction. Hence, the first step to calculate RSS on LPD and TPD is to map the orientation dependence of ' $m$ '.

Figure 7 (a) shows the orientations of various f.c.c. crystallographic directions on the stereographic inverse pole figure (IPF) triangle. Schmid factors were calculated for the  $\{111\} < \bar{1}\bar{1}0 >$  slip system for various grain orientations whose tensile axes are along the directions in Fig. 7 (a). Figs. 7 (b-i) exhibit the tensile axis IPFs mapping Schmid factor distribution for different variants of the slip system  $\{111\} < \bar{1}\bar{1}0 >$  (e.g.  $(111)[\bar{1}\bar{1}0]$ ,  $(\bar{1}10)[101]$  etc.). Note that, ' $m$ ' distributions of 8 variants are mapped in Figs. 7 (b-i). The remaining 4 variants,  $(111)[01\bar{1}]$ ,  $(111)[10\bar{1}]$ ,  $(\bar{1}11)[01\bar{1}]$  and  $(\bar{1}\bar{1}1)[10\bar{1}]$ , have negative/zero ' $m$ ' values for all orientations contained in Fig. 7 (a). The highest Schmid factor is obtained for  $[102]$  tensile axis for the  $(\bar{1}\bar{1}1)[011]$  slip system variant (outlined by black rectangle in Fig. 7 (h)). Interestingly,  $\gamma$  (f.c.c.) grains in the D-pass specimen of CS-HEA (that showed the highest TRIP induced work hardening (Fig. 1 (c)) exhibit a tensile axis IPF with maximum intensity at  $[102]$ , as depicted by Figs. 7 (j) and (k).

The corresponding glide shear strain distribution was also obtained as a function of IPF orientation of tensile axis. Fig. 7 (l) maps a shear strain distribution on IPF that was calculated from Eq. (6) using the assumption that the axial strain is same for all the orientations.

$$\varepsilon = \gamma m \quad (6)$$

where  $\varepsilon$  is the axial strain,  $\gamma$  is the shear strain and  $m$  is the Schmid factor. Thus, the contours on Fig. 7 (j) are an exact replica of the ' $m$ ' distribution IPF Fig. 7 (h), except that the relative intensities are inversely related. Thus,  $[102]$  orientation shows lower strain level than the other orientations, because ' $m$ ' (and hence, RSS) was highest for  $[102]$  in Fig. 7 (h). In reality, the axial strain is also different for the different orientations. Therefore, a more appropriate way to

calculate shear strain dependence of crystallographic orientation is from Eq. (7) [25], using a certain value of global strain,

$$\gamma = \{1/(\sin \chi_0)\}[\{(L_i/L_0)^2 - \sin^2 \lambda_0\}^{1/2} - \cos \lambda_0] \quad (7)$$

where,  $\chi_0$  and  $\lambda_0$  are the angles specifying the orientations of the slip plane and slip direction with respect to the tensile (loading) axis and  $L_i/L_0$  represents the macroscopic engineering strain. The glide shear strain distribution thus obtained for  $(1\bar{1}1)[011]$  slip is plotted on the IPF triangle in Fig. 7 (m). The corresponding axial strain distribution calculated from the shear strain in Fig. 7 (m) is plotted in Fig. 7 (n). Figs. 7 (m-n) indicate higher strain concentration on the ‘hard orientations’ (e.g.  $[112]$  or  $[111]$ ) than ‘soft orientations’ that exhibit high Schmid factor in Fig. 7 (h) (e.g.  $[102]$ ). In short, the quantitative analysis of IPF orientation dependence of ‘m’ reveals that the RSS is highest for  $\{111\} < 1\bar{1}0 >$  slip when the grain is oriented such that its  $<012>$  direction is parallel to the tensile axis. Next, we obtained the RSS on LPD and TPD for the various  $<012>$  directions.

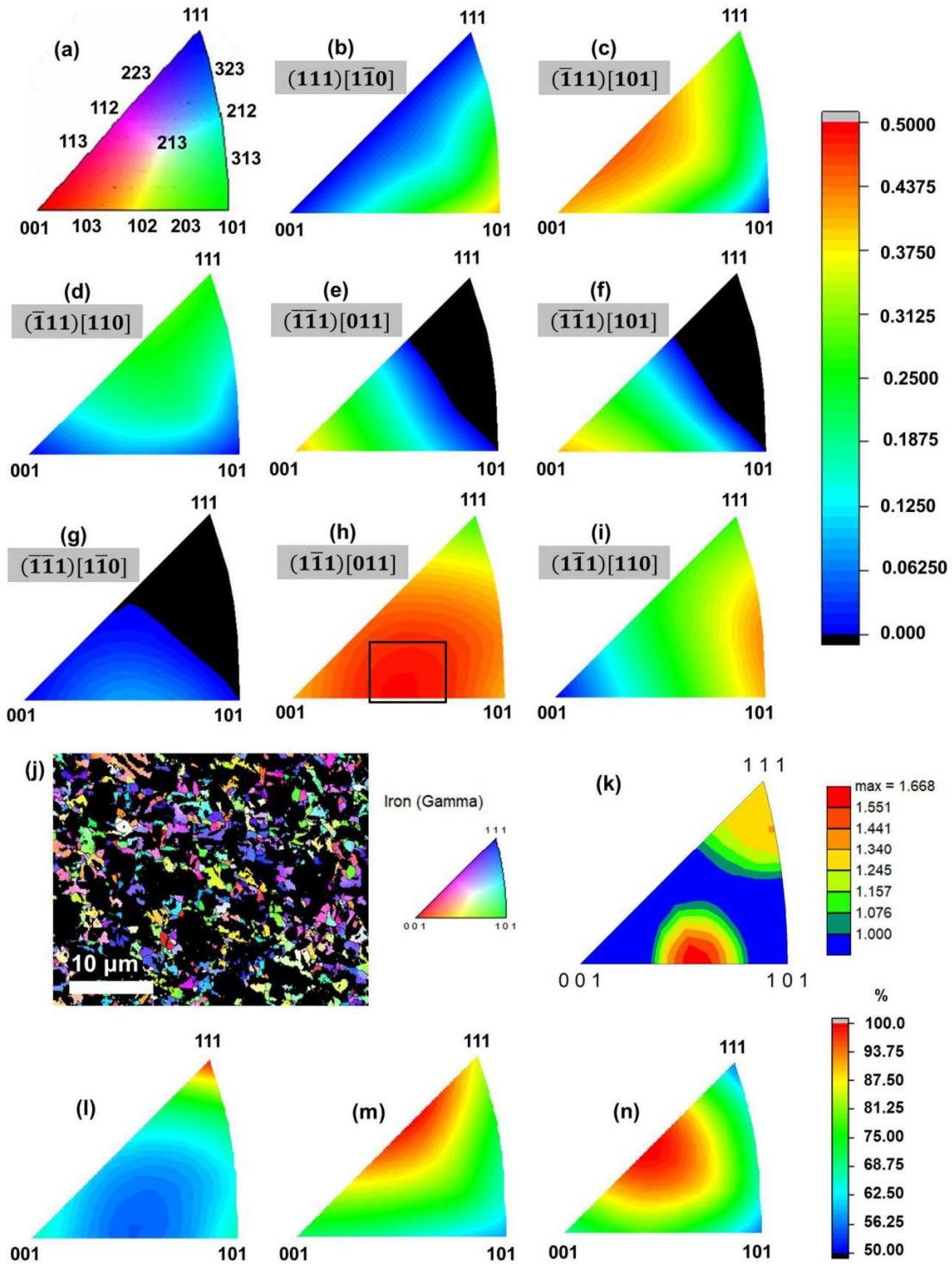


**Fig. 7.** (a) Tensile axis IPF orientations (b-i) Theoretical Schmid factor distributions on IPFs for different variants of  $\{111\} <1\bar{1}0>$  slip system (j) Experimental tensile axis IPF map orientation of  $\gamma$  (f.c.c.) grains in D-pass specimen of CS-HEA and (k) corresponding tensile axis IPF (l-n) Theoretical glide shear strain and axial strain distributions on IPFs. Note that ‘m’

distributions of 8 variants are mapped in (b-i), while the remaining 4 variants  $(111)[0\bar{1}\bar{1}]$ ,  $(111)[10\bar{1}]$ ,  $(\bar{1}11)[01\bar{1}]$  and  $(\bar{1}\bar{1}1)[10\bar{1}]$  have negative/zero ‘m’ values.

### **5.2. Resolved shear stress on partial dislocations and probability of martensitic transformation**

The tensile axis orientations of  $\langle 012 \rangle$  family are superimposed on a 001 stereographic projection of f.c.c. crystal structure in Fig. 8 (a). Note that Fig. 8 (a) is not a pole figure in the true sense of the word. However, since the f.c.c. crystal structure consists of three orthogonal axes that are equal in magnitude, the normal to a plane (pole of the plane) lies along the direction with the same Miller indices. For example, the pole of the  $(111)$  plane is the  $[111]$  direction. Therefore, we can conclude from Fig. 8 (a) that the orientation with the highest RSS is when the tensile axis is perpendicular to one of the planes of  $\{012\}$  family. A pole figure representing the texture with highest RSS would look like Fig. 8 (a). Fig. 8 (b) shows the multiplicity of the tensile axis directions with highest RSS on a 3D Wulff net (since the bottom hemisphere is not revealed in Fig. 8 (a)). The RSS on LPD and TPD for  $[\bar{1}02]$ ,  $[012]$ ,  $[0\bar{1}2]$  and  $[102]$  directions were obtained as a function of the applied tensile flow stress (Figs. 8 (c-f)). Due to symmetry, the RSS on LPD/TPD for the directions in the bottom hemisphere of Fig. 8 (b) are same as the direction of opposite sense in the top hemisphere. The difference in RSS between LPD and TPD increases with applied stress for  $[\bar{1}02]$ ,  $[012]$ ,  $[0\bar{1}2]$ ; only  $[102]$  shows the same RSS for LPD and TPD because both have the same Schmid factor in the latter case.  $[0\bar{1}2]$  shows the highest increase in the difference between RSS of LPD and RSS of TPD with increase in applied stress (Fig. 8 (e)). Hence, grains oriented with  $[0\bar{1}2]$  along the tensile axis would have the highest tendency for separation of partials due to applied stress. Thus, we conclude that  $\gamma$  (f.c.c.) grains oriented with  $[0\bar{1}2] //$  tensile axis would favor deformation induced  $\gamma$  (f.c.c.)  $\rightarrow \varepsilon$  (h.c.p.) transformation.

The elastic force per unit length between two parallel partial dislocations,  $F_{AB}$ , is given by [44],

$$F_{AB} = K(\alpha)/x = Gb_p^2(2 - v)[1 - \{2v\cos 2\alpha/(2 - v)\}]/8\pi x(1 - v) \quad (8)$$

where  $K(\alpha)$  is the elastic force between the partial dislocations,  $x$  is the separation distance between the partials,  $G$  is the shear modulus,  $b_p$  is the Burgers vector of the partial dislocation,  $v$  is the Poisson ratio and  $\alpha$  is the angle between the Burgers vector of the total dislocation. The equilibrium separation between the partial dislocations is given by [44],

$$x_{eqbm} = K(\alpha)/\gamma \quad (9)$$

where  $\gamma$  is the stacking fault energy. This means that for applied stress to increase the separation of the partials, the condition specified by Eq. (9) must be broken so that the leading partial moves farther away from the trailing partial. To restore the equilibrium while the partial dislocation moves, Eq. (10) must be satisfied [44],

$$-K(\alpha)/x + \gamma + (\sigma \cdot \mathbf{b}_p) \cdot \mathbf{n} = 0 \quad (10)$$

where  $\sigma$  is the dyadic representing the applied stress and  $\mathbf{n}$  is the unit vector normal to the slip plane. Since  $(\sigma \cdot \mathbf{b}_p) \cdot \mathbf{n} = \tau b_p$  ( $\tau$  being the shear component of the applied stress on the slip plane in the direction of  $\mathbf{b}_p$ ). Eq. (10) can be written as,

$$-K(\alpha)/x + \gamma + \tau b_p = 0. \quad (11)$$

Thus, we can calculate the critical value of shear component of applied stress required to increase the separation of partial dislocations from Eq. (11). This calculation was performed assuming a partial separation distance of 1  $\mu\text{m}$  and using a SFE of 15 mJ/m<sup>2</sup> because the range of SFE for TRIP is 10-20 mJ/m<sup>2</sup> [45-46]. The critical value of the shear component of applied stress ( $\tau_{\text{crit}}$ ) to increase the partial separation was estimated as 100 MPa. When we plot  $\tau_{\text{crit}}$  on the RSS on LPD/TPD graph (black dotted lines in Figs. 8 (c-f)), we get an estimate of the threshold applied tensile flow stress ( $\sigma_{\text{thr}}$ ) at which  $\gamma$  (f.c.c.) to  $\epsilon$  (h.c.p.) transformation can be triggered by increasing the partial separation for the different <012> tensile directions discussed. The applied stress corresponding to the intersection of  $\tau_{\text{crit}}$  with the RSS on LPD gives  $\sigma_{\text{thr}}$ . The values of  $\sigma_{\text{thr}}$  obtained for  $[\bar{1}02]$ ,  $[012]$  and  $[0\bar{1}2]$  directions are 1312 MPa, 1313 MPa and 731 MPa, respectively (Figs. 8 (c), (d) and (e), respectively). The experimental engineering stress-strain curves for S350, S150 and D-pass specimens were shown in Fig. 1 (b) and the corresponding experimental flow stresses were plotted in Figs. 2 (a), (b) and (c) for S350, S150 and D-pass specimens, respectively. Since the  $\sigma_{\text{thr}}$  values obtained from Figs. 8 (c-e) correspond to flow stresses, they should be compared with the experimental flow stresses in Figs. 2 (a-c). The experimental true yield stresses for S350, S150 and D-pass specimens are 777 MPa, 723 MPa and 657 MPa, respectively (Figs. 2 (a), (b) and (c), respectively). This implies that transformation can be triggered in  $\gamma$  (f.c.c.) grains oriented with its  $[0\bar{1}2]$  crystallographic direction parallel to the tensile loading axis (with  $\sigma_{\text{thr}} = 731$  MPa) at stresses very near to the yield point in these specimens. Further, the engineering plastic strain corresponding to the hump in the strain hardening curve of D-pass specimen is in the range of 0.15-0.2 (Fig. 1 (c)). Taking the engineering plastic strain value of 0.175 within this range, the corresponding engineering stress is 995 MPa for D-pass specimen (Fig. 1 (b)). This corresponds to a true flow stress of 1169 MPa (Fig. 2 (c)). When applied tensile flow stress is increased from  $\sigma_{\text{thr}}$  of  $[0\bar{1}2]$  orientation

(731 MPa) to 1169 MPa, the difference between RSS of LPD and RSS of TPD increases from 100 to 160 MPa (Fig. 8 (e)). Thus, we have quantitatively established through this study that  $\gamma$  (f.c.c.) grains with  $[0\bar{1}2]$  parallel to the tensile loading axis are favorable for undergoing  $\gamma$  (f.c.c.) to  $\epsilon$  (h.c.p.) transformation and the threshold value of applied tensile flow stress for this orientation is 731 MPa.

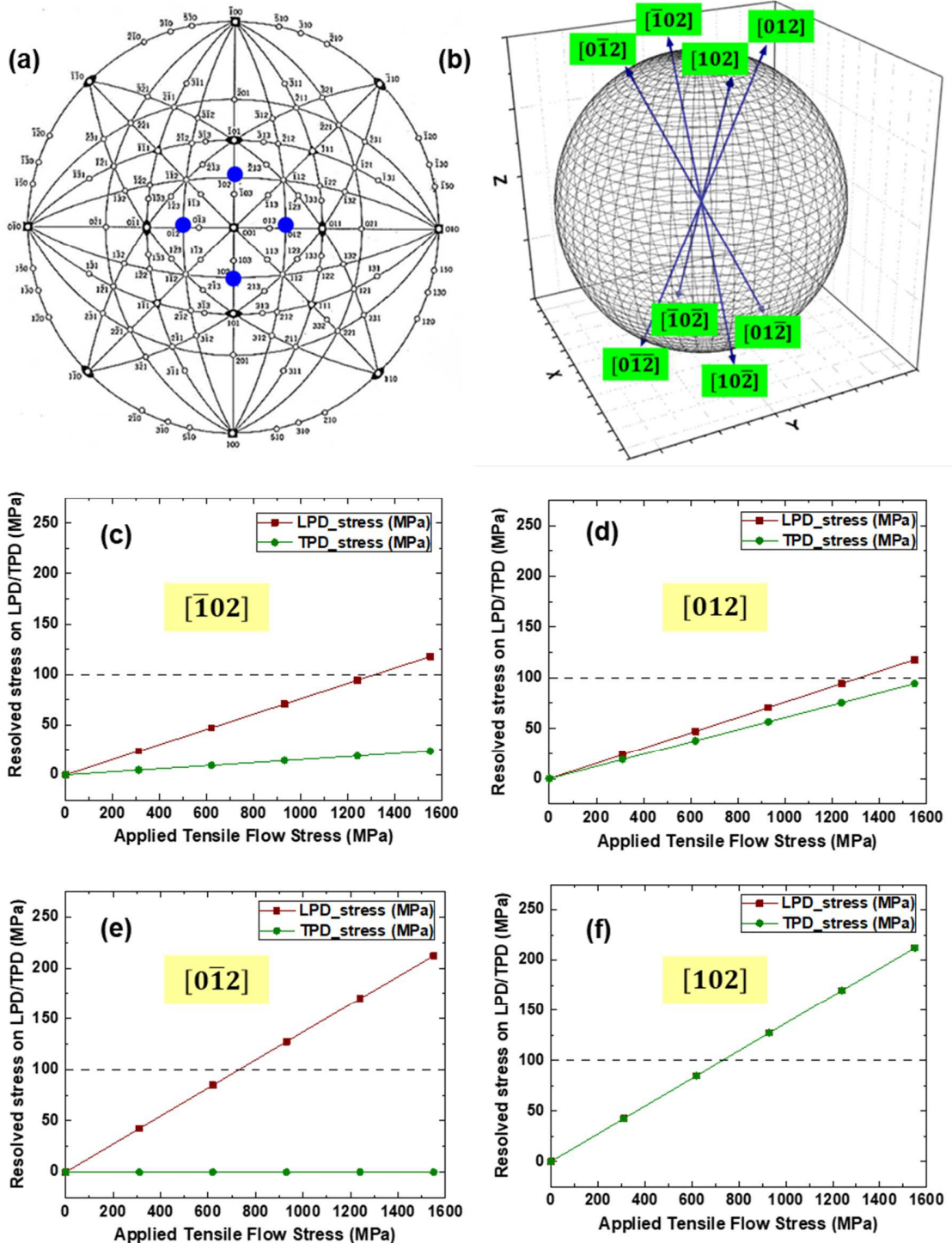


**Fig. 8.** (a) 001 stereographic projection of f.c.c. with superimposed tensile axis orientations with highest resolved shear stress for (111)[011] slip, and (b) multiplicity of the tensile axis orientation in (a) shown on 3D reference sphere. Resolved shear stress on leading and trailing partial dislocations as a function of applied tensile flow stress for (c)  $[1\bar{0}2]$ , (d)  $[012]$ , (e)  $[0\bar{1}2]$ , and (f)  $[102]$  tensile axes.

## 6. Summary

The following conclusions were drawn from the present study of deformation mechanisms and fracture behavior of Fe<sub>40</sub>Mn<sub>20</sub>Co<sub>20</sub>Cr<sub>15</sub>Si<sub>5</sub> HEA (CS-HEA) processed by FSP using different tool rotation rates (S350: single pass at 350 rpm; S150: single pass at 150 rpm; and D-pass: consecutive overlapping passes at 350 and 150 rpm).

1. All three conditions (S350, S150 and D-pass) showed significant uniform elongation but limited non-uniform ductility in quasi-static tensile test. Therefore, a strong microstructural dependence of work hardening behavior due to the additional contribution of TRIP/twin effects differentiates the strength-ductility response of these specimens. Microstructural dependence of fracture initiation is less significant; nevertheless, some differences in the capacity for void nucleation and growth contribute to their propensity for ductile failure after necking.
2. Among the three conditions, D-pass specimen showed the highest additional hardening contribution (~ 500 MPa at UTS) from TRIP/twin effects over and above the contributions of linear Taylor dislocation hardening and geometrical hardening. The crystallographic orientation dependence of resolved shear stress on leading and trailing partial dislocations was quantified to reveal that theoretically,  $\gamma$  (f.c.c.) grains with [012] // tensile axis are favorable for  $\gamma$  (f.c.c.) to  $\epsilon$  (h.c.p.) transformation and the threshold value of applied tensile flow stress for this grain orientation is 731 MPa.
3. Crystal plasticity simulations using VPSC model confirmed that synergistic activity of f.c.c. and h.c.p. deformation modes enabled sustained work hardening by dual-phase strain partitioning in the D-pass specimen, thereby accounting for highest uniform elongation in this specimen.

## Acknowledgments

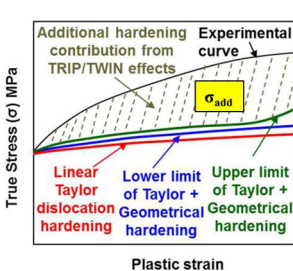
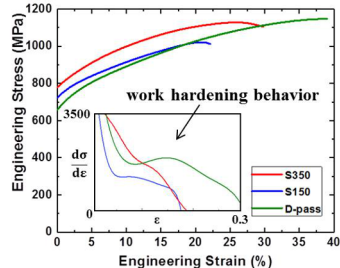
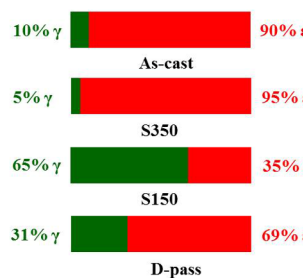
The work was performed under the cooperative agreement of University of North Texas with the U.S. Army Research Laboratory (W911NF-18-2-0067). We thank Materials Research Facility and Advanced Materials and Manufacturing Processes Institute at University of North Texas for access to scanning electron microscopy and X-ray microscopy facilities, respectively. We are grateful to Drs. Hrishikesh Bale, Rachna Parwani and Robin White from Zeiss for training us on the X-ray microscope.

## References

- [1] Z. Li, K.G. Pradeep, Y. Deng, D. Raabe, C.C. Tasan, Metastable high-entropy dual-phase alloys overcome the strength-ductility trade-off, *Nature*, 534 (2016) 227-230.
- [2] Z. Li, D. Raabe, Strong and ductile non-equiatomic high-entropy alloys: Design, processing, microstructure, and mechanical properties, *JOM* 69 (2017) 2099-2106.
- [3] Z. Li, C.C. Tasan, H. Springer, B. Gault, D. Raabe, Interstitial atoms enable joint twinning and transformation induced plasticity in strong and ductile high-entropy alloys, *Sci. Reports*, 7 (2017) 40704-1–40704-7.
- [4] S.S. Nene, K. Liu, M. Frank, R.S. Mishra, R.E. Brennan, K.C. Cho, Z. Li, D. Raabe, Enhanced strength and ductility in a friction stir processing engineered dual phase high entropy alloy, *Sci. Reports*, 7 (2017) 16167-1–16167-7.
- [5] S.S. Nene, M. Frank, K. Liu, R.S. Mishra, B.A. McWilliams, K.C. Cho, Extreme high strength and work hardening ability in a metastable high entropy alloy, *Sci. Reports*, 8 (2018) 9920-1–9920-8.
- [6] S.S. Nene, M. Frank, K. Liu, S. Sinha, R.S. Mishra, B.A. McWilliams, K.C. Cho, Reversed strength-ductility relationship in microstructurally flexible high entropy alloy, *Scripta Mater.*, 154 (2018) 163-167.
- [7] S.S. Nene, S. Sinha, M. Frank, K. Liu, R.S. Mishra, B.A. McWilliams, K.C. Cho, Unexpected strength-ductility response in an annealed, metastable, high-entropy alloy, *Appl. Mater. Today*, 13 (2018) 198-206.
- [8] S. Sinha, S.S. Nene, M. Frank, K. Liu, R.S. Mishra, B.A. McWilliams, K.C. Cho, Microstructural Evolution and Deformation Behavior of Ni-Si-and Co-Si-Containing Metastable High Entropy Alloys, *Met. Mater. Trans. A*, 50 (2019) 179-190.
- [9] L. Lilensten, J-P. Couzinié, J. Bourgon, L. Perrière, G. Dirras, F. Prima, I. Guillot, Design and tensile properties of a bcc Ti-rich high-entropy alloy with transformation-induced plasticity, *Mater. Res. Lett.* 5 (2017) 110-116.
- [10] L. Zhang, H. Fu, S. Ge, Z. Zhu, H. Li, H. Zhang, A. Wang, H. Zhang, Phase transformations in body-centered cubic  $\text{Nb}_x\text{HfZrTi}$  high-entropy alloys, *Mater. Char.* 142 (2018) 443-448.
- [11] S. Wei, J. Kim, C.C. Tasan, Boundary micro-cracking in metastable  $\text{Fe}_{45}\text{Mn}_{35}\text{Co}_{10}\text{Cr}_{10}$  high-entropy alloys, *Acta Mater.* 168 (2019) 76-86.
- [12] Z.C. Luo, M.X. Huang, Revealing the fracture mechanism of twinning-induced plasticity steels, *Steels Res. Int.* 1700433 (2018) 1-7.
- [13] G. Le Roy, J.D. Embury, G. Edwards, M.F. Ashby, A model of ductile fracture based on the nucleation and growth of voids, *Acta Metall.* 29 (1981) 1509-1522.
- [14] V. Tvergaard, A. Needleman, Analysis of the cup-cone fracture in a round tensile bar, *Acta Metall.* 32 (1984) 157-169.
- [15] A. Weck, D.S. Wilkinson, E. Maire, Observation of void nucleation, growth and coalescence in a model metal matrix composite using X-ray tomography, *Mater. Sci. Eng. A* 488 (2008) 435-445.
- [16] P.F. Thomason, Ductile fracture by the growth and coalescence of microvoids of non-uniform size and spacing, *Acta Metall.* 41 (1993) 2127-2134.
- [17] G.I. Taylor, The mechanism of plastic deformation of crystals, *Proc. Roy. Soc. A* 145 (1934) 362-404.
- [18] H. Wiedersich, Hardening mechanisms and the theory of deformation, *JOM* 16 (1964) 425-430.

- [19] H. Mecking, U.F. Kocks, Kinetics of flow and strain-hardening, *Acta Metall.* 29 (1981) 1865-1875.
- [20] U.F. Kocks, H. Mecking, Physics and phenomenology of strain hardening: the FCC case, *Prog. Mater. Sci.* 48 (2003) 171-273.
- [21] K.M. Davoudi, J.J. Vlassak, Dislocation evolution during plastic deformation: Equations vs. discrete dislocation dynamics study, *J. Appl. Phys.* 123 (2018) 085302-1–085302-8.
- [22] T. Takeshita, H-R. Wenk, Plastic anisotropy and geometrical hardening in quartzites, *Tectonophysics* 149 (1988) 345-361.
- [23] M. Miller, P. Dawson, Influence of slip system hardening assumptions on modeling stress dependence of work hardening, *J. Mech. Phys. Solids* 45 (1997) 1781-1804.
- [24] F.F. Lavrentev, The type of dislocation interaction as the factor determining work hardening, *Mater. Sci. Eng.* 46 (1980) 191-208.
- [25] G.E. Dieter, Mechanical Metallurgy, Si Metric Ed. McGraw-Hill Book Company, London, 1988, pp. 127-130.
- [26] R.A. Lebensohn, C.N. Tome, A self-consistent anisotropic approach for the simulation of plastic deformation and texture development of polycrystals: Application to zirconium alloys, *Acta Metall. Mater.* 41 (1993) 2611-2624.
- [27] C.N. Tome, R.A. Lebensohn, Visco-plastic self-consistent (VPSC) Version 7c Manual, 2009.
- [28] C. Tome, G.R. Canova, U.F. Kocks, N. Christodoulou, J.J. Jonas, The relation between macroscopic and microscopic strain hardening in f.c.c. polycrystals, *Acta Metall.* 32 (1984) 1637-1653.
- [29] S. Sinha, J.A. Szpunar, N.A.P. Kiran Kumar, N.P. Gurao, Tensile deformation of 316L austenitic stainless steel using in-situ electron backscatter diffraction and crystal plasticity simulations, *Mater. Sci. Eng. A* 637 (2015) 48-55.
- [30] H. Wang, P.D. Wu, C.N. Tome, J. Wang, Study of lattice strains in magnesium alloy AZ31 based on a large strain elasto-viscoplastic self-consistent polycrystal model, *Int. J. Solids Struct.* 49 (2012) 2155-2167.
- [31] V.M. Miller, T.D. Berman, I.J. Beyerlein, T.M. Pollock, Prediction of magnesium alloy formability: The role of texture, In: *Magnesium Technology* (Eds. A. Singh, K. Solanki, M.V. Manuel, N.R. Neelameggham), Springer, Cham (2016) pp. 257-262.
- [32] S. Sinha, A. Ghosh, N.P. Gurao, Effect of initial orientation on the tensile properties of commercially pure titanium, *Phil. Mag.* 96 (2016) 1485-1508.
- [33] A. Mangal, E.A. Holm, Applied machine learning to predict stress hotspots II: Hexagonal close packed materials, *Int. J. Plast.* 114 (2019) 1-14.
- [34] X. Li, D. L. Irving, L. Vitos, First-principles investigation of the micromechanical properties of fcc-hcp polymorphic high-entropy alloys, *Sci. Reports.* 8 (2018) 11196-1–11196-8.
- [35] P. Yu, L. Zhang, H. Cheng, H. Tang, J. Fan, P.K. Liaw, G. Li, R. Liu, Formation, reverse transformation, and properties of  $\epsilon$ -martensite phase in the CoCrFeMnNi high-entropy alloy under high-pressure, *J. Alloys Compds.* 779 (2019) 1-6.
- [36] K.E.K. Amouzou, T. Richeton, A. Roth, M.A. Lebyodkin, T.A. Lebedkina, Micromechanical modeling of hardening mechanisms in commercially pure  $\alpha$ -titanium in tensile condition, *Int. J. Plast.* 80 (2016) 222-240.
- [37] S. Sinha, N. P. Gurao, In-plane anisotropy in mechanical behavior and microstructural evolution of commercially pure titanium in tensile and cyclic loading, *Met. Mater. Trans. A* 48A (2017) 5813-5832.

- [38] S. Sinha, R.A. Mirshams, T. Wang, S.S. Nene, M. Frank, K. Liu, R.S. Mishra, Nanoindentation behavior of high entropy alloys with transformation-induced plasticity, *Sci. Reports* 9 (2019) 6639-1–6639-11.
- [39] N.P. Gurao, P. Kumar, B. Bhattacharya, A. Haldar, S. Suwas, Evolution of crystallographic texture and microstructure during cold rolling of twinning-induced plasticity (TWIP) steel: Experiments and simulations, *Met. Mater. Trans. A* 43A (2012) 5193-5201.
- [40] M. Frank, Y. Chen, S.S. Nene, S. Sinha, K. Liu, K. An, R.S. Mishra, Investigating the deformation mechanisms of a highly metastable high entropy alloy using in-situ neutron diffraction, Manuscript under revision, *Mater. Today Comm.* (2019).
- [41] P. Noell, J. Carroll, K. Hattar, B. Clark, B. Boyce, Do voids nucleate at grain boundaries during ductile rupture?, *Acta Mater.* 137 (2017) 103-114.
- [42] T.S. Byun, On the stress dependence of partial dislocation separation and deformation microstructure in austenitic stainless steels, *Acta Mater.* 51 (2003) 3063-3071.
- [43] E. Polatidis, W.-N. Hsu, M. Šmíd, T. Panzner, S. Chakrabarty, P. Pant, H. Van Swygenhoven, Suppressed martensitic transformation under biaxial loading in low stacking fault energy metastable austenitic steels, *Scripta Mater.* 147 (2018) 27-32.
- [44] P.B. Hirsch, A. Kelly, Stacking-fault strengthening, *Phil. Mag.* 12 (1965) 881-900.
- [45] S. Martin, S. Wolf, U. Martin, L. Krüger, D. Rafaja, Deformation mechanisms in austenitic TRIP/TWIP steel as a function of temperature, *Met. Mater. Trans. A* 47A (2016) 49-58.
- [46] E.I. Galindo-Nava, P.E.J. Rivera-Díaz-del-Castillo, Understanding martensite and twin formation in austenitic steels: A model describing TRIP and TWIP effects, *Acta Mater.* 128 (2017) 120-134.



$\text{Fe}_{40}\text{Mn}_{20}\text{Co}_{20}\text{Cr}_{15}\text{Si}_5$ (CS-HEA)  
As-cast → As-FSP  
Phase evolution

D-pass specimen shows the highest uniform elongation and sustained work hardening behavior

$\sigma_{add} = 500$  MPa for D-pass  
300 MPa for S350  
200 MPa for S150